Faraday Discussions

Accepted Manuscript

This manuscript will be presented and discussed at a forthcoming Faraday Discussion meeting. All delegates can contribute to the discussion which will be included in the final volume.

Register now to attend! Full details of all upcoming meetings: http://rsc.li/fd-upcoming-meetings

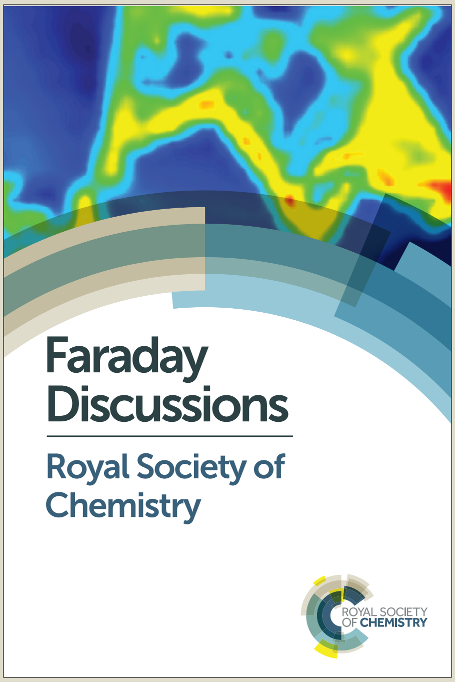

This is an *Accepted Manuscript*, which has been through the Royal Society of Chemistry peer review process and has been accepted for publication.

Accepted Manuscripts are published online shortly after acceptance, before technical editing, formatting and proof reading. Using this free service, authors can make their results available to the community, in citable form, before we publish the edited article. We will replace this *Accepted Manuscript* with the edited and formatted *Advance Article* as soon as it is available.

You can find more information about *Accepted Manuscripts* in the Information for Authors.

Please note that technical editing may introduce minor changes to the text and/or graphics, which may alter content. The journal's standard Terms & Conditions and the Ethical guidelines still apply. In no event shall the Royal Society of Chemistry be held responsible for any errors or omissions in this *Accepted Manuscript* or any consequences arising from the use of any information it contains.

ROYAL SOCIETY
OF CHEMISTRY

www.rsc.org/faraday_d

PAPER www. rsc.org/faraday_d | Faraday Discussions

Interpreting equilibrium-conductivity and conductivity-relaxation measurements to establish thermodynamic and transport properties for multiple charged defect conducting ceramics

Huayang Zhu,[a] Sandrine Ricote,[a] W. Grover Coors,[b] and Robert J. Kee*[a]

Received Xth XXXXXXXXXX 20XX, Accepted Xth XXXXXXXXX 20XX
First published on the web Xth XXXXXXXXXX 200X
DOI: 10.1039/c000000x

A model-based interpretation of measured equilibrium conductivity and conductivity relaxation is developed to establish thermodynamic, transport, and kinetics parameters for multiple charged defect conducting (MCDC) ceramic materials. The present study focuses on 10% yttrium-doped barium zirconate (BZY10). In principle, using the Nernst-Einstein relationship, equilibrium conductivity measurements are sufficient to establish thermodynamic and transport properties. However, in practice it is difficult to establish unique sets of properties using equilibrium conductivity alone. Combining equilibrium and conductivity-relaxation measurements serves to significantly improve the quantitative fidelity of the derived material properties. The models are developed using a Nernst–Planck–Poisson (NPP) formulation, which enables the quantitative representation of conductivity relaxations caused by very large changes in oxygen partial pressure.

1 Introduction

Multiple charged defect conducting (MCDC) ceramics play important roles in mature and emerging technologies. For example, solid-oxide fuel cell (SOFC) cathodes are often fabricated using mixed ionic-electronic conducting (MIEC) materials such as lanthanum strontium cobalt ferrite (LSCF). The present effort is concerned primarily with yttrium-doped barium zirconates (BZY), which have interesting proton-conducting properties. These materials can be used in intermediate-temperature (i.e., around 500 °C) protonic-ceramic fuel cells (PCFC) or electrolyzers.[1–4] Other emerging applications include hydrogen separations and catalytic membrane reactors.[5–7]

---

[a] *Mechanical Engineering, Colorado School of Mines, Golden, CO, USA. Fax: 303-273-3602; Tel: 303-273-3379; E-mail: rjkee@mines.edu*
[b] *CoorsTek, Inc., Golden, CO, USA.*

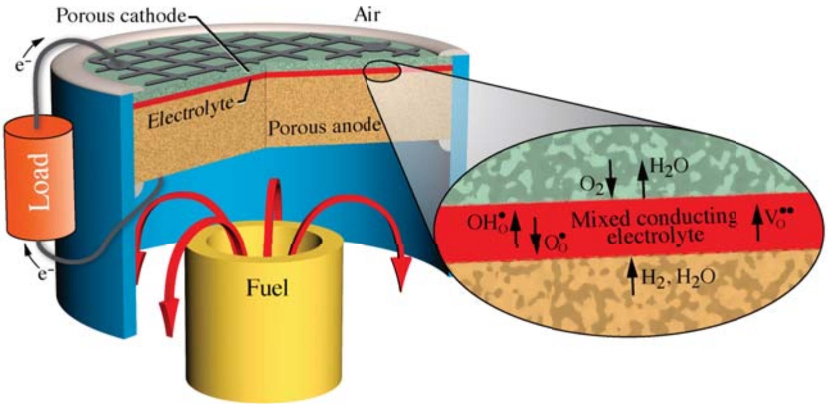

Fig. 1 Illustration of a proton-conducing solid-oxide fuel cell (PCFC) in a button-cell configuration

Figure 1 illustrates a PCFC configured as a button cell. The fuel compartment is on the lower anode side and air is on the upper cathode side. The ion transport through the MCDC electrolyte membrane is fundamentally different from a traditional SOFC with an oxide-ion-conducting electrolyte membrane. As illustrated in the balloon inset of Fig. 1, protonic defects ($OH_O^{\bullet}$) are conducted via a Grotthuss mechanism from the fuel side toward the oxidizer side. In a mixed conductor such as BZY, there is a counter flux of oxide-ion vacancies and “holes.” As discussed subsequently, the holes are assumed to be small polarons that are associated with oxygen sites on the doped perovskite crystal lattice. To make clear that the holes are polarons, the O-site polarons are designated as $O_O^{\bullet}$. In BZY, the oxide-ion vacancies are typically minority charge carriers.

Unlike in an SOFC, the oxidation product H_2O is produced primarily in the cathode chamber of a PCFC, potentially leading to improved efficiency. Nevertheless, because the MCDC electrolyte permits some oxide-ion transport, low levels of H_2O can be formed in the anode chamber. Moreover, because there is some electronic conductivity in the mixed-conducting electrolyte membrane, the leakage current contributes to efficiency loss. The MCDC materials tend to have reasonable proton conductivity at relatively intermediate temperatures (i.e., around 500 - 600 °C). The intermediate-temperature performance potentially leads to system-level improvements in terms of materials selections, catalyst degradation, sealing strategies, etc.

The present paper draws a clear distinction between MIEC and MCDC materials. As discussed by Riess[8], MIEC materials permit electronic conduction via band-state holes or electrons. Certain ceramic materials (e.g., doped ceria, doped barium zirconate) generally do not have metallic-type electronic conduction. Nevertheless, previous literature frequently refers to “hole” mobility and MIEC behavior. Such nomenclature is used, even in cases where the “holes” are stated to be small polarons. The “holes” are understood to be small polarons that are associated with the lattice oxygen. Thus, it is reasonable to introduce a new nomenclature (MCDC), making clear that none of the charge-carrying defects have band-state behavior.

Despite the current and potential importance of the MCDC ceramics, there are surprisingly few quantitatively predictive modeling capabilities that can be applied in technology design and process optimization. Because the MCDC materials typically have three or more charged-defects (e.g., protonic defects, oxide ions, small polarons), widely-practiced models such as this based on ambipolar diffusion are not directly applicable. The Nernst–Planck–Poisson formulation is applicable, but computationally more complex than ambipolar diffusion.[9–12]

The present experimental and modeling approaches generally follow the one developed recently to establish thermodynamic and transport properties in doped ceria.[13,14] However, ceria has only two charge-carrying defects (oxide ions and reduced-cerium polarons). Thus, for MCDC materials such as BZY the task is significantly more complex because three charge-carrying defects must be considered.

The overarching objective of the present investigation is to develop experimental and modeling approaches that can be applied to establish thermodynamic and transport properties for MCDC ceramics. The needed thermodynamic properties are the changes in enthalpy ΔH° and entropy ΔS° for each defect-incorporation reaction at the ceramic-gas interface. The needed transport properties are diffusion coefficients for each of the defects within the MCDC ceramic. The transport properties are represented as a pre-exponential factors and an activation energy.

The conductivity-relaxation experiments reveal kinetic limitations associated with the defect reactions at the MCDC-gas interfaces. Thus, in addition to establishing thermodynamic and transport properties, the model-based experimental interpretation leads to quantitative insight about the surface kinetics. The surface kinetics are represented as microscopically reversible reactions, with the forward and reverse rates being constrained by the thermodynamic equilibrium constants.

2 Experimental approach

2.1 Rod preparation

The extruded BZY10 rods were fabricated by solid state reactive sintering (SSRS) using precursor oxides and sulfates: Barium sulfate–Blanc Fixe (Solvay Chemicals, Inc, $BaSO_4$), zirconium oxide (Neo Performance Materials (AMR Ltd), $\geq$99.5% ZrO_2), cerium oxide (Neo Performance Materials (AMR Ltd) 99.5% CeO_2), yttrium oxide (HJD Intl. 99.99+% ultra-fine Y_2O_3). The appropriate amounts of precursors were mixed with 1.0 wt% of black nickel oxide (Novomet, Grade F NiO[*]) and ball milled in deionized water for 24 hours. The mixture was subsequently dried in air and sieved through a 40 mesh screen. The resulting powder was blended with water-soluble acrylic and a cellulosic-ether plasticizer and pelletized for wet-extrusion processing. Green rods were extruded through an encapsulated die set, producing unfired rods with a diameter of 6.3 mm. The rods were dried and then hang-fired in air at 1600 °C for 6 hours. The fired shrinkage was about 31%, producing a fired diameter of 4.3 mm.

Alumina was used as a getter for NiO extraction from dense fired monolithic pellets of SSRS BZY10. The sintered dense rods were buried in Almatis calcined

---

[*] D50 of 1-2 microns. Weight-percent impurities: Co<0.0015; Fe<0.015; Cu<0.001; S<0.001

---

alumina (CT3000LS SG) inside an alumina crucible and re-fired at 1600 °C for 20 hours. Following NiO extraction, the rods were removed from the packed powder and surface ground to remove any surface-reaction layers that may have developed by reaction with the alumina powder during Ni-extraction process. The grinding and polishing process reduced the rod diameter to 3 mm.

Finally, the samples were subjected to a 24-hour annealing process. For the annealing process, samples were placed on ceramic foam filter of SELEE® structure in a sealed alumina tube and heated in air to 800 °C at 5 °C min^{-1}. Once the furnace temperature reached 800 °C, hydrogen forming gas (4% H_2, balance argon) was added to the chamber at a rate of 1000 mL min^{-1} and exhausted to atmosphere for 24 hours. Platinum leads were attached at the ends of the rod, painted with Pt paste and fired at 1100 °C for 2 h.

2.2 Testing protocol

Because the experimental procedures have been previously reported,[13] only a brief summary is included here. Figure 2 illustrates the experimental setup in which solid slender rods of BZY10 are placed within a furnace under controlled temperature and gas composition. The rods are approximately 3 mm in diameter and 20 mm long. This somewhat unusual configuration offers some important advantages compared to other sample configurations. Under conductivity-relaxation conditions (i.e., rapidly switching the gas environment) the defect transport is effectively one-dimensional in the radial direction while the conductivity measurement is essentially one-dimensional in the axial direction. As reported previously,[14] one-dimensional radial models can be developed to assist quantitative data interpretation. Such models are relatively straightforward to solve computationally, even with very large variations in the gas-phase atmospheres.

The gas flow rates used in the experiments were sufficient to ensure defect equilibrium with the rod surfaces, but not so high as to introduce an axial temperature gradient in the specimen. Equilibrium conductivity measurements were made after the rod achieved equilibrium in a particular gas atmosphere. All the gases were either dried through Drierite ($CaSO_4$) or humidified through bubblers maintained at room temperature (approximately 3.8% humidification or $p_{H_2O} \approx 3154$ Pa, assuming laboratory atmospheric pressure of 0.83 atm.). Following the Drierite, the H_2O partial pressure is estimated to be 10 ppm. To avoid water condensation, all the lines were heated to about 50 °C. The oxygen partial pressure was measured in the exhaust gas using a zirconia p_{O_2} sensor fabricated by CoorsTek. The p_{O_2} sensor was maintained at the same temperature as the sample chamber.

Alternating current electrochemical impedance spectra (EIS) were recorded as a function of temperature and oxygen partial pressure at frequencies ranging from 20 Hz to 1 MHz, with an amplitude of 0.1 V using an Hewlett Packard 4284A Precision LCR Meter interfaced with LABVIEW.† Figure 3 shows typical EIS measurements represented as Nyquist plots together with single-arc RQ fits. The ZSIMPWIN software‡ was used to fit equivalent-circuit representations of the

---

† National Instruments, Inc.

‡ Princeton Applied Research

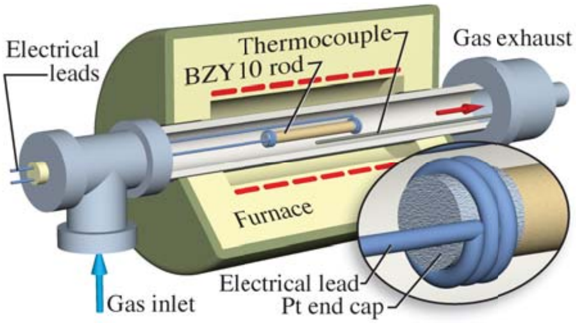

Fig. 2 Experimental configuration of measuring equilibrium conductivity and conductivity relaxation

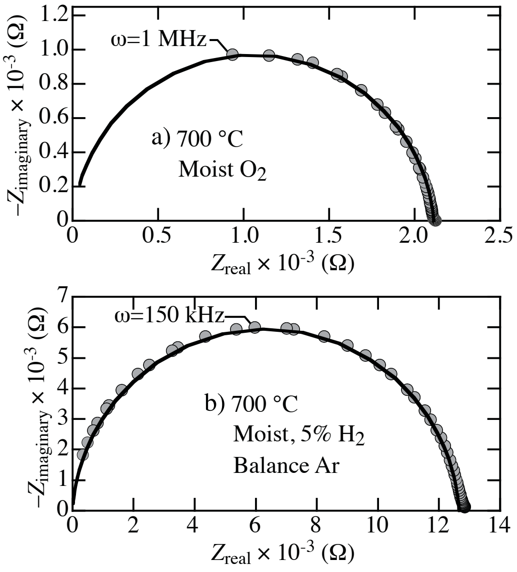

Fig. 3 Nyquist representation of typical electrochemical impedance measurements and RQ fits

measured AC spectra.

Under equilibrium conditions, the conductivity is measured using RQ fits to full EIS sweeps. However, to measure conductivity relaxation, full EIS sweeps are impractical. Fortunately, as shown in Table 1, it is possible to identify and monitor a single frequency (here 500 Hz under dry conditions, and 5 kHz under moist conditions) during the relaxation from which the transient conductivity can be measured with errors not exceeding 0.5%. It should be noted that the single frequency is not related to any particular characteristic of the Nyquist plot such as the summit frequency.

Table 1 Comparison of steady-state resistances based on full EIS sweeps and at a single frequency at different temperatures and gas compositions. The “error” columns represent the differences between the resistances measured by the full EIS sweep and those measured at single specified frequencies.

Temperature (°C)	*R* (Ω) (RQ fit)	*R* (Ω) (500 Hz)	error (%)	Temperature (°C)	*R* (Ω) (RQ fit)	*R* (Ω) (5 kHz)	error (%)
Dry, O_2				Moist 3.8% H_2O, O_2			
600	3,602	3,605	0.08	600	6,447	6,415	0.49
700	1,469	1,469	0.00	700	2,113	2,108	0.23
800	794	789	0.60	800	980	979	0.10
Dry, 1% O_2, balance Ar				Moist 3.8% H_2O, 1% O_2, balance Ar			
600	7,961	7,969	0.10	600	9,568	9,575	0.07
700	3,461	3,463	0.06	700	4,527	4,510	0.37
800	1,804	1,805	0.05	800	2,096	2,093	0.14
Dry, 5% H_2, balance Ar				Moist 3.8% H_2O, 5% H_2, balance Ar			
600	199,000	198,000	0.50	600	15,140	15,160	0.13
700	97,030	97,040	0.01	700	12,660	12,675	0.11
800	107,000	106,600	0.37	800	11,730	11,705	0.20

2.3 Testing sequence

Because of slow dehydration within the rod, the testing follows a certain sequence from dry to moist conditions. The prepared rod (Section 2.1) was placed into the testing apparatus (Fig. 2), whereupon it was heated in dry (through drierite) 100 mL $\min^{-1}$ of Argon to 800 °C, while recording the resistance. When the resistance reached a constant value (after about 3 days, slow dehydration), AC spectra were collected in dry atmospheres (both oxidizing and reducing) as a function of temperature. After having determined the particular frequency for conductivity-relaxation measurements (in this case 500 Hz), the resistance was recorded during the relaxation transient when switching from dry 100% O_2 to dry 1% O_2 (balance Ar) and vice versa, at 600, 700 and 800 °C.

Following experiments in dry environments, the atmosphere was humidified with a bubbler maintained at room temperature (approximately 3.8% H_2O) and a similar procedure was followed: first AC spectra at equilibrium were collected in both oxidizing and reducing atmospheres as a function of temperature and then conductivity relaxations (at 5 kHz) were recorded at 600, 700 and 800 °C when switching back and forth from moist O_2 to moist 1% O_2.

3 Defect chemistry

In our foregoing BZY models[10–12] we assumed four possible charge-carrying defects, protons $OH_O^\bullet$, oxide vacancies $V_O^{\bullet\bullet}$, electron holes $h^\bullet$, and electrons e'. Using Kröger–Vink notation, these defects at the surface are assumed to interact with the gas environment according to four defect reactions as

$$\frac{1}{2}\mathrm{H_2} + \mathrm{O_O^\times} \rightleftharpoons \mathrm{OH_O^\bullet} + \mathrm{e'} \tag{1}$$

$$\frac{1}{2}\mathrm{O_2} + \mathrm{V_O^{\bullet\bullet}} \rightleftharpoons \mathrm{O_O^\times} + 2\mathrm{h^\bullet} \tag{2}$$

$$\mathrm{H_2O} + \mathrm{V_O^{\bullet\bullet}} + \mathrm{O_O^\times} \rightleftharpoons 2\mathrm{OH_O^\bullet} \tag{3}$$

$$\mathrm{null} \rightleftharpoons \mathrm{h^\bullet} + \mathrm{e'} \tag{4}$$

The holes and electrons are understood to be small polarons, not delocalized or band-state electronic charge carriers. In practice, the models show that although electrons are included, they are essentially negligible for BZY materials.

3.1 Alternative defect reactions

Stokes and Islam[15] proposed that the "holes" are small polarons localized at the oxygen sites, which may be modeled as $\mathrm{O^-}$. The present study assumes that a delocalized hole $\mathrm{h^\bullet}$ associated with an oxygen site can be represented as

$$\mathrm{O_O^\times} + \mathrm{h^\bullet} \rightleftharpoons \mathrm{O_O^\bullet}. \tag{5}$$

The (perhaps unusual) nomenclature $\mathrm{O_O^\bullet}$ designates a hole (polaron) localized at an oxygen site. The nomenclature is intended to be analogous with $\mathrm{OH_O^\bullet}$, meaning a protonic defect associated with an oxygen site. The combination of Reactions 2 and 5 yields an alternative form of the oxygen-incorporation reaction as

$$\frac{1}{2}\mathrm{O_2} + \mathrm{V_O^{\bullet\bullet}} + \mathrm{O_O^\times} \rightleftharpoons 2\mathrm{O_O^\bullet}. \tag{6}$$

Thus, Reaction 6 differs from Reaction 2 by twice the association energy of the oxygen-bound polaron relative to an (unbound) valance-band hole.

Stokes and Islam also suggested that electrons would be localized on a metal site. In this case, Reaction 1 might be rewritten as

$$\frac{1}{2}\mathrm{H_2} + \mathrm{O_O^\times} + \mathrm{Zr_{Zr}^\times} \rightleftharpoons \mathrm{OH_O^\bullet} + \mathrm{Zr'_{Zr}}. \tag{7}$$

Then, Reaction 4 can be rewritten as,

$$\mathrm{O_O^\times} + \mathrm{Zr_{Zr}^\times} \rightleftharpoons \mathrm{O_O^\bullet} + \mathrm{Zr'_{Zr}}. \tag{8}$$

For BZY10, the electrons are not favored thermodynamically even in reducing environments, and can be assumed to be immediately annihilated in favor of a hole. By combining Reactions 7 and 8, the resulting hydrogen-incorporation reaction would be rewritten as

$$\frac{1}{2}\mathrm{H_2} + \mathrm{O_O^\bullet} \rightleftharpoons \mathrm{OH_O^\bullet}. \tag{9}$$

which would eliminate the need for Reaction 4 or 8.

3.2 Defect-reaction equilibrium and kinetics

The reformulated defect reactions for BZY10 consider only three charge-carrying defects – protons $\mathrm{OH_O^{\bullet}}$, oxygen vacancies $\mathrm{V_O^{\bullet\bullet}}$, and O-site polarons $\mathrm{O_O^{\bullet}}$. The three defect reactions at the ceramic-gas interface can be summarized as

$$\frac{1}{2}\mathrm{H_2} + \mathrm{O_O^{\bullet}} \underset{k_{\mathrm{b,H_2}}}{\overset{k_{\mathrm{f,H_2}}}{\rightleftharpoons}} \mathrm{OH_O^{\bullet}}, \tag{10}$$

$$\frac{1}{2}\mathrm{O_2} + \mathrm{O_O^{\times}} + \mathrm{V_O^{\bullet\bullet}} \underset{k_{\mathrm{b,O_2}}}{\overset{k_{\mathrm{f,O_2}}}{\rightleftharpoons}} 2\mathrm{O_O^{\bullet}}, \tag{11}$$

$$\mathrm{H_2O} + \mathrm{V_O^{\bullet\bullet}} + \mathrm{O_O^{\times}} \underset{k_{\mathrm{b,H_2O}}}{\overset{k_{\mathrm{f,H_2O}}}{\rightleftharpoons}} 2\mathrm{OH_O^{\bullet}}. \tag{12}$$

The present study considers that these reactions may be equilibrated or may be kinetically rate controlled. If the reactions proceed at finite rates, microscopic reversibility is enforced (i.e., forward and backward rates are related through the equilibrium constants). If the reactions are maintained at equilibrium, then, assuming gas-phase equilibrium, one of the reactions is redundant.

The forward and backward rate expressions are denoted as $k_{\mathrm{f},i}$ and $k_{\mathrm{b},i}$. The defect production rates at the gas-surface interface can be represented as

$$\dot{s}_{\mathrm{O_O^{\bullet}}} = 2\dot{q}_{\mathrm{O_2}} - \dot{q}_{\mathrm{H_2}}, \tag{13}$$

$$\dot{s}_{\mathrm{V_O^{\bullet\bullet}}} = -\dot{q}_{\mathrm{O_2}} - \dot{q}_{\mathrm{H_2O}}, \tag{14}$$

$$\dot{s}_{\mathrm{OH_O^{\bullet}}} = 2\dot{q}_{\mathrm{H_2O}} + \dot{q}_{\mathrm{H_2}}, \tag{15}$$

$$\dot{s}_{\mathrm{O_O^{\times}}} = -\dot{q}_{\mathrm{O_2}} - \dot{q}_{\mathrm{H_2O}}, \tag{16}$$

where the gas-phase reaction rates of progress can be reprinted as

$$\dot{q}_{\mathrm{O_2}} = k_{\mathrm{f,O_2}}[\mathrm{V_O^{\bullet\bullet}}][\mathrm{O_O^{\times}}][\mathrm{O_2}]^{1/2} - k_{\mathrm{b,O_2}}[\mathrm{O_O^{\bullet}}]^2, \tag{17}$$

$$\dot{q}_{\mathrm{H_2}} = k_{\mathrm{f,H_2}}[\mathrm{O_O^{\bullet}}][\mathrm{H_2}]^{1/2} - k_{\mathrm{b,H_2}}[\mathrm{OH_O^{\bullet}}], \tag{18}$$

$$\dot{q}_{\mathrm{H_2O}} = k_{\mathrm{f,H_2O}}[\mathrm{V_O^{\bullet\bullet}}][\mathrm{O_O^{\times}}][\mathrm{H_2O}] - k_{\mathrm{b,H_2O}}[\mathrm{OH_O^{\bullet}}]^2. \tag{19}$$

The equilibrium constants, written in terms of molar concentrations, can be stated as

$$K_{\mathrm{c,O_2}} = \frac{k_{\mathrm{f,O_2}}}{k_{\mathrm{b,O_2}}} = \frac{[\mathrm{O_O^{\bullet}}]^2}{[\mathrm{V_O^{\bullet\bullet}}][\mathrm{O_O^{\times}}][\mathrm{O_2}]^{1/2}} = K_{\mathrm{p,O_2}}\left[\frac{p_{\mathrm{atm}}}{RT}\right]^{-1/2}, \tag{20}$$

$$K_{\mathrm{c,H_2}} = \frac{k_{\mathrm{f,H_2}}}{k_{\mathrm{b,H_2}}} = \frac{[\mathrm{OH_O^{\bullet}}]}{[\mathrm{O_O^{\bullet}}][\mathrm{H_2}]^{1/2}} = K_{\mathrm{p,H_2}}\left[\frac{p_{\mathrm{atm}}}{RT}\right]^{-1/2}, \tag{21}$$

$$K_{\mathrm{c,H_2O}} = \frac{k_{\mathrm{f,H_2O}}}{k_{\mathrm{b,H_2O}}} = \frac{[\mathrm{OH_O^{\bullet}}]^2}{[\mathrm{V_O^{\bullet\bullet}}][\mathrm{O_O^{\times}}][\mathrm{H_2O}]} = K_{\mathrm{p,H_2O}}\left[\frac{p_{\mathrm{atm}}}{RT}\right]^{-1}. \tag{22}$$

The equilibrium constants K_p based on the gas-phase partial pressures and lattice formula-unit concentrations are defined as

$$K_{p,\mathrm{H_2}} = \frac{[\mathrm{OH_O^\bullet}]_\mathrm{L}}{p_\mathrm{H_2}^{1/2}[\mathrm{O_O^\bullet}]_\mathrm{L}}, \tag{23}$$

$$K_{p,\mathrm{O_2}} = \frac{[\mathrm{O_O^\bullet}]_\mathrm{L}^2}{p_\mathrm{O_2}^{1/2}\,[\mathrm{O_O^\times}]_\mathrm{L}\,[\mathrm{V_O^{\bullet\bullet}}]_\mathrm{L}}, \tag{24}$$

$$K_{p,\mathrm{H_2O}} = \frac{[\mathrm{OH_O^\bullet}]_\mathrm{L}^2}{p_\mathrm{H_2O}\,[\mathrm{O_O^\times}]_\mathrm{L}\,[\mathrm{V_O^{\bullet\bullet}}]_\mathrm{L}}. \tag{25}$$

The formula-unit concentrations $[X_k]_\mathrm{L}$ are related to the molar concentrations $[X_k]$ via the molar volume V_m as $[X_k]_\mathrm{L} = [X_k]V_\mathrm{m}$. For BZY10, the lattice molar volume is $V_\mathrm{m} = 44.792 \times 10^{-6}$ m^3 mol^{-1}. The three equilibrium constants $K_{p,\mathrm{H_2}}$, $K_{p,\mathrm{O_2}}$ and $K_{p,\mathrm{H_2O}}$ are not independent, but are coupled through the gas-phase equilibrium constant $K_{p,\mathrm{G}}$ as

$$K_{p,\mathrm{H_2}}^2 K_{p,\mathrm{O_2}} = K_{p,\mathrm{H_2O}} K_{p,\mathrm{G}}. \tag{26}$$

The present model assumes that the gas phase is maintained in equilibrium according to

$$\mathrm{H_2} + \frac{1}{2}\mathrm{O_2} \rightleftharpoons \mathrm{H_2O}, \tag{27}$$

with $K_{p,\mathrm{G}}$ being the equilibrium constant.

All the equilibrium constants can be evaluated from the Gibbs free energy change for the reactions $\Delta G^\circ = \Delta H^\circ - T\Delta S^\circ$ as

$$K_p = \exp\left(-\frac{\Delta G^\circ}{RT}\right) = \exp\left(\frac{\Delta S^\circ}{R}\right)\exp\left(-\frac{\Delta H^\circ}{RT}\right). \tag{28}$$

The gas-phase thermodynamics are well known; for reaction 27 $\Delta H^\circ = -241.11$ kJ mol^{-1} and $\Delta S^\circ = -55.48$ J mol^{-1} K^{-1}. Thermodynamic parameters for the defect reactions will be determined using the conductivity measurements.

3.3 Site and electroneutrality constraints

On the surface and within the ceramic, site constraints and electroneutrality must be preserved. The number of oxygen sites in a pervoskite lattice (per formula unit) must be maintained as 3. Thus,

$$[\mathrm{V_O^{\bullet\bullet}}]_\mathrm{L} + [\mathrm{OH_O^\bullet}]_\mathrm{L} + [\mathrm{O_O^\bullet}]_\mathrm{L} + [\mathrm{O_O^\times}]_\mathrm{L} = 3. \tag{29}$$

In this formulation, Eq. 29 is written to include the O-site polaron $[\mathrm{O_O^\bullet}]_\mathrm{L}$ in the site constraint. However, it may be questioned as to whether the electronic defect (i.e., polaron) "occupies" the site in the same sense as an ionic defect (i.e., an atom or vacancy) does. If the defect were a delocalized band hole, then it would not enter the oxygen site balance.

Charge neutrality requires that

$$2[\mathrm{V_O^{\bullet\bullet}}]_\mathrm{L} + [\mathrm{OH_O^\bullet}]_\mathrm{L} + [\mathrm{O_O^\bullet}]_\mathrm{L} - [\mathrm{Y'_{Zr}}]_\mathrm{L} = 0. \tag{30}$$

Considering BZY10 ($\mathrm{BaZr_{0.9}Y_{0.1}O_{3-\delta}}$), the doping concentration is 10%, in which case $[\mathrm{Y'_{Zr}}]_\mathrm{L} = 0.1$.

3.4 Defect equilibrium concentrations

The defect equilibrium concentrations ($[\mathrm{V}_{\mathrm{O}}^{\bullet\bullet}]_{\mathrm{L}}$, $[\mathrm{OH}_{\mathrm{O}}^{\bullet}]_{\mathrm{L}}$, $[\mathrm{O}_{\mathrm{O}}^{\bullet}]_{\mathrm{L}}$, and $[\mathrm{O}_{\mathrm{O}}^{\times}]_{\mathrm{L}}$) on the surface are functions of the gas-phase partial pressures (p_{O_2}, p_{H_2}, and $p_{\mathrm{H}_2\mathrm{O}}$) and can be established by solving iteratively Eqs. 24, 25, 29, and 30. Note that Eq 23 is not used because Eqs. 23, 24, and 25 are not independent of each other, but are coupled through the gas-phase equilibrium (Eq. 26).

The iteration process is initiated by first estimating a value of $[\mathrm{V}_{\mathrm{O}}^{\bullet\bullet}]_{\mathrm{L}}$. Based on Eqs. 24, 25, and 30, the defect concentrations $[\mathrm{O}_{\mathrm{O}}^{\bullet}]_{\mathrm{L}}$ and $[\mathrm{OH}_{\mathrm{O}}^{\bullet}]_{\mathrm{L}}$ can be evaluated in terms of $[\mathrm{V}_{\mathrm{O}}^{\bullet\bullet}]_{\mathrm{L}}$ as

$$[\mathrm{O}_{\mathrm{O}}^{\bullet}]_{\mathrm{L}} = \frac{[\mathrm{Y}'_{\mathrm{Zr}}]_{\mathrm{L}} - 2[\mathrm{V}_{\mathrm{O}}^{\bullet\bullet}]_{\mathrm{L}}}{1+\Theta}, \tag{31}$$

$$[\mathrm{OH}_{\mathrm{O}}^{\bullet}]_{\mathrm{L}} = \Theta[\mathrm{O}_{\mathrm{O}}^{\bullet}]_{\mathrm{L}}, \tag{32}$$

where

$$\Theta = \frac{[\mathrm{OH}_{\mathrm{O}}^{\bullet}]_{\mathrm{L}}}{[\mathrm{O}_{\mathrm{O}}^{\bullet}]_{\mathrm{L}}} = \left[\frac{K_{p,\mathrm{H}_2\mathrm{O}}}{K_{p,\mathrm{O}_2}}\frac{p_{\mathrm{H}_2\mathrm{O}}}{p_{\mathrm{O}_2}^{1/2}}\right]^{1/2}. \tag{33}$$

Using Eq. 24, $[\mathrm{O}_{\mathrm{O}}^{\times}]_{\mathrm{L}}$ can be represented as

$$[\mathrm{O}_{\mathrm{O}}^{\times}]_{\mathrm{L}} = \frac{[\mathrm{O}_{\mathrm{O}}^{\bullet}]_{\mathrm{L}}^2}{K_{p,\mathrm{O}_2} p_{\mathrm{O}_2}^{1/2}[\mathrm{V}_{\mathrm{O}}^{\bullet\bullet}]_{\mathrm{L}}}. \tag{34}$$

Finally, the oxygen site constraint (Eq. 29) is imposed. If all the equations above were to be explicitly substituted, the result would be one nonlinear equation with one unknown, $[\mathrm{V}_{\mathrm{O}}^{\bullet\bullet}]_{\mathrm{L}}$. Once $[\mathrm{V}_{\mathrm{O}}^{\bullet\bullet}]_{\mathrm{L}}$ is determined, all the other defect concentrations follow easily from Eqs. 31, 32, and 34.

4 Nernst–Planck–Poisson model

To model conductivity relaxations quantitatively, the spatial and temporal variations in defect concentrations are governed by conservation equations as

$$\frac{\partial[X_k]}{\partial t} + \nabla\cdot\mathbf{J}_k = 0, \tag{35}$$

where the Nernst–Planck fluxes can be written as

$$\mathbf{J}_k = -D_k\left(\nabla[X_k] + \frac{z_k F}{RT}[X_k]\nabla\Phi\right). \tag{36}$$

The electrostatic-potential profiles Φ are determined by solving the Gauss equation,

$$\nabla\cdot(\varepsilon_{\mathrm{r}}\varepsilon_{\mathrm{o}}\nabla\Phi) = -\rho_{\mathrm{e}} = -F\sum_{k=1}^{K} z_k[X_k]. \tag{37}$$

The relative and vacuum permittivities are represented as ε_{r} and ε_{o}, respectively. The local charge density is represented as ρ_{e}. Boundary conditions for the defect concentrations are established in terms of the surface reactions. The boundary condition for the electrostatic potential is established in terms of a zero net charge transfer at the ceramic surface. Details of the Nernst–Planck–Poisson (NPP) model and the computational solution can be found elsewhere.[10]

As discussed previously,[13] the experimental configuration (Fig. 2) has been designed such that the NPP problem can be solved in one-dimensional radial coordinates. Although there are inevitably some end effects near the end electrodes, two-dimensional axisymmetric models show that that the one-dimensional approximation is valid.

5 Parameter fitting algorithm

Altogether, twelve (ten independent) parameters are needed to characterize the BZY10 material. Specifically, ΔH° and ΔS° are needed for each of the three defect reactions (Eqs. 10-12). Because the thermodynamics of the defect reactions are correlated through the gas-phase equilibrium, only four of these thermodynamic parameters are independent. The defect diffusion coefficients are represented in Arrhenius form as $D_k = D_k^\circ \exp(-E_k/RT)$. Thus, two parameters ($D_k^\circ$ and E_k) are needed to describe the diffusion coefficients for each of the three mobile charged defects ($\mathrm{V}_\mathrm{O}^{\bullet\bullet}$, $\mathrm{OH}_\mathrm{O}^{\bullet}$, and $\mathrm{O}_\mathrm{O}^{\bullet}$).

The fitting process begins with a least-squares fit of measured equilibrium conductivities, using measurements from a wide range of oxygen partial pressures and temperatures. The Nernst-Einstein equation (Eq. 38) forms the basis for this fitting process. Very good fits can be obtained in the sense that a set of parameters can be found that matches the data well. The problem is one of non-uniqueness. That is, alternative sets of different parameters do an equally good job of matching the equilibrium data.

The consideration of conductivity-relaxation data provides additional information that is valuable in resolving ambiguities associated with considering equilibrium conductivities alone. Using the parameter set from an initial fit to equilibrium conductivity measurements, the NPP model is used to predict relaxation profiles. In the first instance, the defect-incorporation reactions are assumed to be in equilibrium with the gas-phase environment, providing the boundary conditions for the NPP model. However, the initial set of parameters from the equilibrium fits usually do not lead to good representations of the measured relaxations. Often the predicted relaxation times (based on surface equilibrium) are slower than the measured relaxation, which cannot be correct. In other words, surface equilibration should produce relaxation times that are shorter than the measured relaxations. Thus, parameter adjustments are needed to assure that the modeled relaxations under surface equilibrium are no slower than the data. With adjusted parameters, the equilibrium fits are repeated, making sure that the equilibrium data is still represented accurately.

It is usually the case that after the thermodynamic and transport parameters are established, the model-predicted relaxation times are faster that the measurements for the reducing-to-oxidizing relaxations. This indicates a surface-reaction kinetic limitation. Thus, the next step is to establish forward rate expressions for the surface kinetics (i.e., reactions 10-12). The reverse rates are constrained by microscopic reversibility, involving the thermodynamic equilibrium constant and hence the thermodynamic fitting parameters. Thus, the kinetic limitations also provide information that is important to establishing the thermodynamic and transport parameters.

5.1 Equilibrium fits

Assuming a dilute limit, measurable conductivity σ is related to defect concentrations $[X_k]$ and diffusion coefficients D_k via the Nernst-Einstein relationship as

$$\sigma = \sum \sigma_k = \frac{F^2}{RT} \sum_{k=1}^{K} z_k^2 [X_k] D_k, \tag{38}$$

where σ_k are partial conductivities of the participating defects. In this expression F and R are the Faraday and gas constants, respectively, and z_k are the charges associated with the mobile defects. At equilibrium, the defect concentrations are established by reactions with the gas phase at the ceramic surface, and hence thermodynamic Gibbs free energy associated each reaction. The diffusion coefficients are represented in Arrhenius form as $D_k = D_k^\circ \exp(-E_k/RT)$.

The experimentally measured conductivities σ_i^* over a range of oxygen partial pressures p_{O_2} and temperature T can be used to determine ten physical parameters (i.e., four thermodynamic parameters: $\Delta H^\circ_{\mathrm{H_2O}}$, $\Delta H^\circ_{\mathrm{O_2}}$, $\Delta S^\circ_{\mathrm{H_2O}}$, and $\Delta S^\circ_{\mathrm{O_2}}$, and six transport parameters: $D^\circ_{\mathrm{OH}^\bullet_\mathrm{O}}$, $D^\circ_{\mathrm{V}^{\bullet\bullet}_\mathrm{O}}$, $D^\circ_{\mathrm{O}^\bullet_\mathrm{O}}$, $E_{\mathrm{OH}^\bullet_\mathrm{O}}$, $E_{\mathrm{V}^{\bullet\bullet}_\mathrm{O}}$, and $E_{\mathrm{O}^\bullet_\mathrm{O}}$) by minimizing the following residual function:

$$\min_{\mathbf{S}} \sum_{i=1}^{N} \left(\ln \sigma_i - \ln \sigma_i^*\right)^2. \tag{39}$$

In this expression the vector $\mathbf{S}$ represents all the fitting parameters, and N is the total number of measured conductivities. The nonlinear least-squares fitting problem is implemented here using the "lsqnonlin" function in MATLAB.

Using Eq. 26, the enthalpy and entropy changes associated with the hydrogen-incorporation reaction (Eq. 1) can be obtained from the fitting thermodynamic parameters as

$$\Delta H^\circ_{\mathrm{H_2}} = (\Delta H^\circ_{\mathrm{G}} + \Delta H^\circ_{\mathrm{H_2O}} - \Delta H^\circ_{\mathrm{O_2}})/2, \tag{40}$$

$$\Delta S^\circ_{\mathrm{H_2}} = (\Delta S^\circ_{\mathrm{G}} + \Delta S^\circ_{\mathrm{H_2O}} - \Delta S^\circ_{\mathrm{O_2}})/2. \tag{41}$$

In these expressions, $\Delta H^\circ_{\mathrm{G}}$ and $\Delta S^\circ_{\mathrm{G}}$ refer to the gas-phase equilibrium reaction (i.e., Eq. 27).

In principle, the equilibrium conductivity measurements and Eq. 38 are sufficient to determine all the fit parameters. However, the "best" fits are usually found to predict some parameter values that conflict with independently established values. Also, there are significant ambiguities in the sense that many different combinations of parameters produce nearly equivalent representations of the measured conductivities. The following section develops a set of "unconstrained" fits. Then, certain parameters are fixed based on independent information, producing a set of "constrained" fits.

5.2 Unconstrained parameter fits

Assuming that there are no constraints for the fitting parameters, Fig. 4 compares the measured (filled circles) and modeled (dashed lines) equilibrium conductivities as functions of p_{O_2} at the temperatures of 600, 700, and 800 °C and 0.829

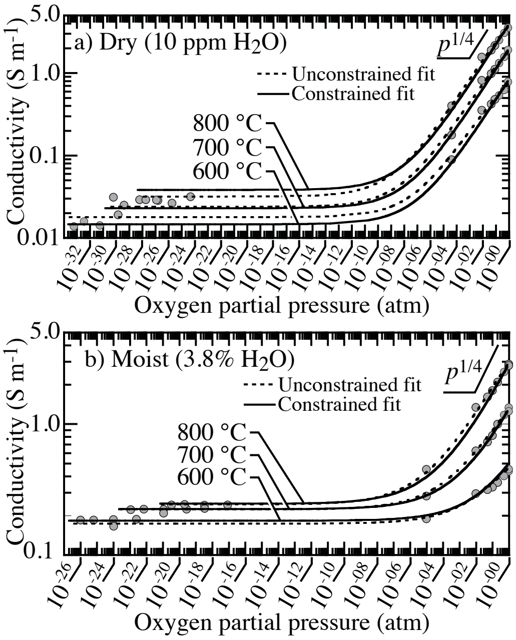

Fig. 4 Comparison of the model predictions (solid lines for constrained fits, and dashed lines for unconstrained fits) with the measured conductivities (filled circles) at 600 °C, 700 °C, and 800 °C as functions of p_{O_2}. The gas-phase environment is a mixture of H_2, O_2, H_2O, and Ar, producing a wide range of oxygen partial pressures. a) Dry gas-phase environment (10 ppm H_2O). b) Moist gas-phase environment (3.8% H_2O).

atm total pressure. The oxygen partial pressure p_{O_2} is evaluated assuming an equilibrium gas-phase mixture of H_2, O_2, H_2O, and Ar. By comparing Figs. 4a and 4b, it is clear that moisture significantly increases conductivity in the reducing regions, but tends to decrease the conductivity in the oxidizing regions. As illustrated in Fig. 4, the measured equilibrium conductivities can be reasonably well represented by the model over wide ranges of temperature and p_{O_2}. Table 2 shows thermodynamic and transport parameters for the unconstrained and constrained fits, with the constrained fitting being discussed in the following section.

5.3 Constrained parameter fits

Assuming that the gas-phase environment is pure Ar, then $[\mathrm{O}_\mathrm{O}^\bullet]_\mathrm{L} = 0$ and $[\mathrm{OH}_\mathrm{O}^\bullet]_\mathrm{L} = 0$. The charge-neutrality constraint (Eq. 30) leads to $[\mathrm{V}_\mathrm{O}^{\bullet\bullet}]_\mathrm{L} = [\mathrm{Y}'_\mathrm{Zr}]_\mathrm{L}/2$. In the Ar environment, the total conductivity can be represented as

$$\sigma = \frac{z^2_{\mathrm{V}_\mathrm{O}^{\bullet\bullet}} F^2}{RT} \frac{[X_{\mathrm{V}_\mathrm{O}^{\bullet\bullet}}]_\mathrm{L}}{V_\mathrm{m}} D_{\mathrm{V}_\mathrm{O}^{\bullet\bullet}} = \frac{z^2_{\mathrm{V}_\mathrm{O}^{\bullet\bullet}} F^2}{RT} \frac{[\mathrm{Y}'_\mathrm{Zr}]_\mathrm{L}}{2V_\mathrm{m}} D^\circ_{\mathrm{V}_\mathrm{O}^{\bullet\bullet}} \exp\left(-\frac{E_{\mathrm{V}_\mathrm{O}^{\bullet\bullet}}}{RT}\right). \qquad (42)$$

Fig. 5 shows the measured temperature-dependent conductivity in the Ar environment, which can be fit using $D^\circ_{\mathrm{V}_\mathrm{O}^{\bullet\bullet}} = 1.43 \times 10^{-7}$ m^2 s^{-1} and $E_{\mathrm{V}_\mathrm{O}^{\bullet\bullet}} \approx 67$ kJ mol^{-1}. However, the experimental Ar gas mixture actually contains impurities of

Table 2 Thermodynamic and transport parameters that result from constrained and unconstrained fits

	Thermodynamic parameters					
	$\Delta H^\circ_{O_2}$	$\Delta H^\circ_{H_2O}$	$\Delta H^\circ_{H_2}$	$\Delta S^\circ_{O_2}$	$\Delta S^\circ_{H_2O}$	$\Delta S^\circ_{H_2}$
		(kJ mol^{-1})			(J mol^{-1} K^{-1})	
Unconstrained	-41.56	-96.65	-151.60	-73.45	-90.30	-36.17
Constrained	-36.08	-80.00	-146.01	-125.48	-71.78	-0.89

	Transport parameters					
	$E_{O_O^\bullet}$	$E_{OH_O^\bullet}$	$E_{V_O^{\bullet\bullet}}$	$D^\circ_{O_O^\bullet}$	$D^\circ_{OH_O^\bullet}$	$D^\circ_{V_O^{\bullet\bullet}}$
		(kJ mol^{-1})			(m^2 s^{-1})	
Unconstrained	85.05	41.79	43.38	5.95×10^{-05}	2.22×10^{-08}	7.51×10^{-10}
Constrained	86.00	35.09	67.00	1.70×10^{-03}	9.38×10^{-09}	1.30×10^{-08}

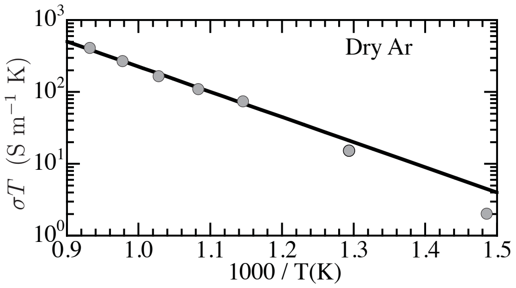

Fig. 5 Comparison of the model prediction (solid lines) with the experimentally measured total conductivity (filled circles) at functions of temperature. The gas-phase mixture contains Ar with 10 ppm H_2O and 50 ppm O_2.

approximately 10 ppm H_2O and 50 ppm O_2. Consequently, the oxygen-vacancy diffusion coefficient $D^\circ_{V_O^{\bullet\bullet}}$ cannot be accurately evaluated, and is retained as a parameter in the fitting algorithm. But, $E_{V_O^{\bullet\bullet}} = 67$ kJ mol^{-1} is fixed.

There is general consensus in the literature[16–18] that $\Delta H^\circ_{H_2O} \approx 80$ kJ mol^{-1}. Therefore, in the fitting process $\Delta H^\circ_{H_2O}$ is constrained to be 80 kJ mol^{-1}. Additionally, based on the relaxation analysis discussed in later sections, $E_{O_O^\bullet} \approx 86$ kJ mol^{-1} and $D^\circ_{O_O^\bullet} \approx 1.70 \times 10^{-3}$ m^2 s^{-1} are also fixed. Figure 4 shows that the measured equilibrium conductivity can also be fit reasonably well using these constrained parameters. All the fitting parameters are listed in Table 2. Compared to the unconstrained fitting parameters, the O-site polaron diffusivity $D_{O_O^\bullet}$ resulting from the constrained fitting is about 25 times larger than it is in the unconstrained fit, which is critical for the model to capture the conductivity relaxation processes.

5.4 Conductivity relaxation

As a practical matter, all the thermodynamic and transport parameters cannot be fit uniquely based on the measured equilibrium conductivity alone. Fortunately, the conductivity-relaxation measurements can provide additional data that assist

Table 3 End-point gas-phase mole-fraction compositions for the conductivity relaxations

	Reducing				Oxidizng			
	H_2	O_2	H_2O	Ar	H_2	O_2	H_2O	Ar
DryOx	0	0.01000	0.00001	0.98999	0	0.99999	0.00001	0
MoistOx	0	0.00962	0.03774	0.95264	0	0.96226	0.03774	0
MoistRedox	0.04811	0.00005	0.03774	0.91410	0	0.96226	0.03774	0

Table 4 Comparison of measured and modeled relaxation times τ (seconds)

		Reducing to oxidizing			Oxidizing to reducing		
	T (°C)	Expr	Equil	Kinetic	Expr	Equil	Kinetic
DryOx	600	7224	4250	5440	6179	2760	5940
	700	1824	1640	1940	2233	1150	2320
	800	545	660	780	980	480	910
MoistOx	600	492	130	380	486	125	850
	700	462	90	220	449	75	520
	800	308	70	140	350	54	310
MoistRedox	600	21462	145	5490	69	118	202
	700	3500	100	2580	185	56	132
	800	1823	80	1480	92	30	99

establishing the needed physical parameters.

The conductivity-relaxation measurements begin from an equilibrium state under a particular gas-phase composition and temperature. The relaxation is initiated by switching rapidly from one gas-phase environment (e.g., low p_{O_2}) to another gas-phase environment (e.g., high p_{O_2}), and vice versa.[13] The relaxation is complete when the rod's conductivity reaches equilibrium with the final gas-phase environment. As listed in Table 3, the present study considers three initial and final gas-phase compositions. The relaxation sets are named "DryOx," "MoistOx," and "MoistRedox." Each relaxation experiment is repeated for three temperatures – 600, 700 and 800 °C. Thus, altogether eighteen relaxation experiments are considered. In all cases the total pressure is 0.829 atm (atmospheric pressure in Denver).

To be quantitative, the characteristic conductivity-relaxation time τ is taken to be the time needed for the conductivity to achieve 95% of the final steady-state conductivity after the suddenly switching between gas-phase environments. Table 4 lists the measured and modeled relaxation times. As shown in Table 4, the relaxation time for all the cases decreases as the temperature increases. The relaxation time from 1% to 100% O_2 is shorter than it is from 100% to 1% O_2 under both the dry and moist conditions, but the times are comparable at each temperature. However, introducing moisture into the oxidizing environment can significantly shorten the relaxation time. The moist H_2 reducing-to-oxidizing relaxation times are significantly longer than the characteristic times in the oxidizing-to-reducing direction.

5.5 Approximate ambipolar diffusion

When applicable, ambipolar diffusion is practically useful. An important aspect of the utility is that the important effects of internal electrostatic-potential fields are subsumed into the ambipolar diffusion coefficients, and thus do not need to be explicitly considered. Consequently, the mathematics appear as a pure diffusion problem.[12] However, the resulting ambipolar diffusion coefficient depends nonlinearly on the defect concentrations, the ordinary diffusion coefficients, and the defect charges.

Ambipolar-diffusion concepts are strictly limited to only two mobile charge carriers, but the ambipolar concepts can be used to assess qualitatively, and even quantitatively, the relative importance of individual defect diffusion coefficients. For instance, by neglecting the transport contribution from $\mathrm{V}_\mathrm{O}^{\bullet\bullet}$, the ambipolar diffusion coefficient $\mathcal{D}_{\mathrm{O}_\mathrm{O}^\bullet-\mathrm{OH}_\mathrm{O}^\bullet}$ based on the ionic pair $\mathrm{O}_\mathrm{O}^\bullet$ and $\mathrm{OH}_\mathrm{O}^\bullet$ can be defined as[12]

$$\mathcal{D}_{\mathrm{O}_\mathrm{O}^\bullet-\mathrm{OH}_\mathrm{O}^\bullet} \equiv \frac{\left(z_{\mathrm{OH}_\mathrm{O}^\bullet}^2[\mathrm{OH}_\mathrm{O}^\bullet]+z_{\mathrm{O}_\mathrm{O}^\bullet}^2[\mathrm{O}_\mathrm{O}^\bullet]\right)D_{\mathrm{OH}_\mathrm{O}^\bullet}D_{\mathrm{O}_\mathrm{O}^\bullet}}{z_{\mathrm{OH}_\mathrm{O}^\bullet}^2 D_{\mathrm{OH}_\mathrm{O}^\bullet}[\mathrm{OH}_\mathrm{O}^\bullet]+z_{\mathrm{O}_\mathrm{O}^\bullet}^2 D_{\mathrm{O}_\mathrm{O}^\bullet}[\mathrm{O}_\mathrm{O}^\bullet]}. \tag{43}$$

Although ambipolar diffusion coefficients vary spatially and nonlinearly during transients, relaxation times can be estimated as $\tau \approx R_\mathrm{out}^2/\mathcal{D}_{\mathrm{O}_\mathrm{O}^\bullet-\mathrm{OH}_\mathrm{O}^\bullet}$, where the ambipolar diffusion coefficient is evaluated at the rod's surface ($r = R_\mathrm{out}$). For example, assuming a relaxation time of $\tau \approx 100$ s from the MoistRedox oxidizing-to-reducing environment at 800 °C, $\mathcal{D}_{\mathrm{O}_\mathrm{O}^\bullet-\mathrm{OH}_\mathrm{O}^\bullet} \approx 2.2 \times 10^{-8}$ m^2 s^{-1}. Similarly, considering a relaxation time of $\tau \approx 550$ s at 800 °C from 1% to 100% O_2 under dry conditions, $\mathcal{D}_{\mathrm{O}_\mathrm{O}^\bullet-\mathrm{V}_\mathrm{O}^{\bullet\bullet}} \approx 4.1 \times 10^{-9}$ m^2 s^{-1}.

It is interesting to understand why the ambipolar diffusion coefficient evaluated at the rod surface is particularly relevant for estimating the relaxation time. Beginning with the entire rod being in equilibrium with a gas-phase environment, the gas environment is suddenly changed. Consequently, the defect concentrations at the rod surface rapidly comes into equilibrium with the new gas-phase environment. The new defect concentrations must “diffuse” into the rod interior, ultimately bringing the entire rod into equilibrium with the new gas-phase environment. Thus, it is the ambipolar diffusion coefficients associated with the new gas-phase environment that control the characteristic transport, and hence relaxation, times.

Following some algebraic manipulation, the ambipolar diffusion coefficient as stated in Eq. 43 can be rewritten as

$$\frac{1}{\mathcal{D}_{\mathrm{O}_\mathrm{O}^\bullet-\mathrm{OH}_\mathrm{O}^\bullet}} = \frac{1}{D_{\mathrm{OH}_\mathrm{O}^\bullet}\left(1+\frac{z_{\mathrm{OH}_\mathrm{O}^\bullet}^2}{z_{\mathrm{O}_\mathrm{O}^\bullet}^2}\frac{[\mathrm{OH}_\mathrm{O}^\bullet]}{[\mathrm{O}_\mathrm{O}^\bullet]}\right)} + \frac{1}{D_{\mathrm{O}_\mathrm{O}^\bullet}\left(1+\frac{z_{\mathrm{O}_\mathrm{O}^\bullet}^2}{z_{\mathrm{OH}_\mathrm{O}^\bullet}^2}\frac{[\mathrm{O}_\mathrm{O}^\bullet]}{[\mathrm{OH}_\mathrm{O}^\bullet]}\right)}, \tag{44}$$

which reveals that

$$\mathcal{D}_{\mathrm{O}_\mathrm{O}^\bullet-\mathrm{OH}_\mathrm{O}^\bullet} \leq \min\left\{D_{\mathrm{OH}_\mathrm{O}^\bullet}\left(1+\frac{[\mathrm{OH}_\mathrm{O}^\bullet]}{[\mathrm{O}_\mathrm{O}^\bullet]}\right), D_{\mathrm{O}_\mathrm{O}^\bullet}\left(1+\frac{[\mathrm{O}_\mathrm{O}^\bullet]}{[\mathrm{OH}_\mathrm{O}^\bullet]}\right)\right\}. \tag{45}$$

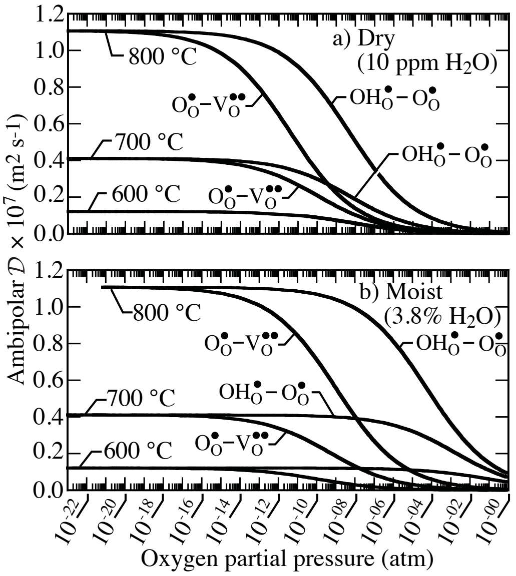

Fig. 6 Ambipolar diffusion coefficients at 600 °C, 700 °C, and 800 °C as functions of p_{O_2} for defect pairs $\mathrm{O_O^\bullet} - \mathrm{OH_O^\bullet}$ and $\mathrm{O_O^\bullet} - \mathrm{V_O^{\bullet\bullet}}$ under dry and moist environments.

In highly reducing environments, $[\mathrm{O_O^\bullet}]/[\mathrm{OH_O^\bullet}] \ll 1$, leading to

$$\mathcal{D}_{\mathrm{O_O^\bullet}-\mathrm{OH_O^\bullet}} \le \min\left\{ D_{\mathrm{O_O^\bullet}}, D_{\mathrm{OH_O^\bullet}} \frac{[\mathrm{OH_O^\bullet}]}{[\mathrm{O_O^\bullet}]} \right\}. \tag{46}$$

To achieve the $\mathcal{D}_{\mathrm{O_O^\bullet}-\mathrm{OH_O^\bullet}} \approx 2.2 \times 10^{-8}$ m^2 s^{-1}, which was estimated for the MoistRedox oxidizing-to-reducing relaxation at 800 °C, the ordinary diffusion coefficient for the O-site polaron must be $D_{\mathrm{O_O^\bullet}} \ge 2.2 \times 10^{-8}$ m^2 s^{-1}. Using parameters from the unconstrained fits (Table 2), $D_{\mathrm{O_O^\bullet}} \approx 4.31 \times 10^{-9}$ m^2 s^{-1} at 800 °C. Thus, it is unlikely that the measured relaxation behaviors can be captured by the unconstrained fitting parameters.

Figure 6 illustrates the behavior of the ambipolar diffusion coefficients for BZY10 over a wide range of oxygen partial pressures and temperatures for moist and dry conditions. The ambipolar diffusion coefficient $\mathcal{D}_{\mathrm{OH_O^\bullet}-\mathrm{V_O^{\bullet\bullet}}}$ is not shown here because $\mathcal{D}_{\mathrm{OH_O^\bullet}-\mathrm{V_O^{\bullet\bullet}}}$ is two orders of magnitude smaller than $\mathcal{D}_{\mathrm{O_O^\bullet}-\mathrm{OH_O^\bullet}}$ and $\mathcal{D}_{\mathrm{O_O^\bullet}-\mathrm{V_O^{\bullet\bullet}}}$ and nearly independent of p_{O_2}. It is evident that the functional forms of $\mathcal{D}_{\mathrm{O_O^\bullet}-\mathrm{OH_O^\bullet}}$ i and $\mathcal{D}_{\mathrm{O_O^\bullet}-\mathrm{V_O^{\bullet\bullet}}}$ are qualitatively and quantitatively similar. Higher temperatures contribute to higher ambipolar diffusion coefficients, thus suggesting faster relaxations at higher temperatures. At a particular temperature, the values of $\mathcal{D}_{\mathrm{O_O^\bullet}-\mathrm{OH_O^\bullet}}$ and $\mathcal{D}_{\mathrm{O_O^\bullet}-\mathrm{OH_O^\bullet}}$ approach each other under both very reducing and very oxidizing conditions, but are separated in between. In oxidizing regions and at a given oxygen partial pressure, higher moisture levels tend to increase the ambipolar diffusion coefficients.

The binary-pair ambipolar diffusion coefficients provide substantial insight about the relaxation processes. One observation is that the relatively mobile polaron $\mathrm{O_O^\bullet}$ plays an important role in relaxation processes. Because the ambipolar diffusion coefficients in the reducing environments are higher than those in the oxidizing environments, the relaxation times from the oxidizing environment should be shorter than those from the reducing environment to oxidizing environment. In fact, this is the measured result (cf., Table 4).

5.6 Relaxation-based parameter adjustment

The O-site polaron transport is found to be closely coupled with the thermodynamics ($\Delta H^\circ_{\mathrm{O}_2}$ and $\Delta S^\circ_{\mathrm{O}_2}$) of the oxygen-incorporation reaction (Eq. 11). Thus, it is interesting to explore the relationships in the context of equilibrium conductivity and conductivity relaxation. Using a range fixed values for $E_{\mathrm{O}_\mathrm{O}^\bullet}$, lower-limit values for $D^\circ_{\mathrm{O}_\mathrm{O}^\bullet}$ are set such that the NPP model using equilibrium defect reactions on the surface matches the relaxation curve from 1% to 100% O_2 under dry conditions at 800 °C. With these parameters fixed, it is also found that all the other relaxation times predicted by the surface-equilibrated NPP model are at least faster than the measurements, which is the desired result.

5.7 Influence of $E_{\mathrm{O}_\mathrm{O}^\bullet}$

The O-site polaron transport has a strong influence on relaxation times. Thus, it is interesting to investigate the effects of $D_{\mathrm{O}_\mathrm{O}^\bullet}$ on all other fitting parameters by systematically varying the diffusion activation energy $E_{\mathrm{O}_\mathrm{O}^\bullet}$. Specifically, as listed in Table 5, six values of $E_{\mathrm{O}_\mathrm{O}^\bullet}$ are considered, and the $D^\circ_{\mathrm{O}_\mathrm{O}^\bullet}$ values are readjusted such that the model based on the equilibrium defect reactions achieve essentially the same relaxation time as with $E_{\mathrm{O}_\mathrm{O}^\bullet} = 86$ kJ mol^{-1}. In this study, two other parameters are fixed as $\Delta H^\circ_{\mathrm{H_2O}} = 80$ kJ mol^{-1} and $E_{\mathrm{V}_\mathrm{O}^{\bullet\bullet}} = 67$ kJ mol^{-1}. Table 5 compares the resulting thermodynamic and transport parameters.

Table 5 shows that the some parameters depend only weakly on $E_{\mathrm{O}_\mathrm{O}^\bullet}$, but others depend strongly. The transport parameters ($D^\circ_{\mathrm{OH}_\mathrm{O}^\bullet}$, $D^\circ_{\mathrm{V}_\mathrm{O}^{\bullet\bullet}}$, and $E_{\mathrm{OH}_\mathrm{O}^\bullet}$), as well as $\Delta S^\circ_{\mathrm{H_2O}}$ have only weak dependence. Two parameters show strong dependence, which provides insight for estimating the value of the polaron transport activation energy, $E_{\mathrm{O}_\mathrm{O}^\bullet}$. In the range $65 \leq E_{\mathrm{O}_\mathrm{O}^\bullet} \leq 90$ kJ mol^{-1}, the oxygen-incorporation enthalpy $\Delta H^\circ_{\mathrm{O}_2}$ decreases from nearly zero to approximately -44 kJ mol^{-1}. In the same range, the entropy associated with the hydrogen incorporation $\Delta S^\circ_{\mathrm{H}_2}$ increases from approximately -20 J mol^{-1} K^{-1} to being slightly positive. On physical grounds, the oxygen incorporation is expected to be exothermic[19,20] and the H_2 incorporation entropy should remain negative. These considerations bound the acceptable range of $E_{\mathrm{O}_\mathrm{O}^\bullet}$. Although certainly not entirely definitive, the present study uses $E_{\mathrm{O}_\mathrm{O}^\bullet} = 86$ kJ mol^{-1}. This choice makes the oxygen incorporation as exothermic as possible, but does not permit the hydrogen-incorporation entropy to become positive. The other thermodynamic and transport parameters that result from the choice of $E_{\mathrm{O}_\mathrm{O}^\bullet}$ are listed in the corresponding rows of Table 5. These parameters are at least consistent with prior literature, satisfy physical constraints, and provide a good representation of all the measurements reported herein.

Table 5 Thermodynamic and transport parameters as functions of $E_{\mathrm{O}_\mathrm{O}^\bullet}$

Thermodynamic parameters

$E_{\mathrm{O}_\mathrm{O}^\bullet}$	$\Delta H^\circ_{\mathrm{O}_2}$	$\Delta H^\circ_{\mathrm{H_2O}}$	$\Delta H^\circ_{\mathrm{H}_2}$	$\Delta S^\circ_{\mathrm{O}_2}$	$\Delta S^\circ_{\mathrm{H_2O}}$	$\Delta S^\circ_{\mathrm{H}_2}$
(kJ mol^{-1})		(kJ mol^{-1})			(J mol^{-1} K^{-1})	
65	6.31	-80.00	-167.21	-85.98	-71.78	-20.64
70	-3.76	-80.00	-162.17	-95.37	-71.78	-15.95
75	-13.85	-80.00	-157.13	-104.77	-71.78	-11.25
80	-23.94	-80.00	-152.08	-114.17	-71.78	-6.55
85	-34.05	-80.00	-147.03	-123.60	-71.78	-1.84
86	-36.08	-80.00	-146.01	-125.48	-71.78	-0.89
90	-44.18	-80.00	-141.96	-133.03	-71.78	2.88

Transport parameters

$E_{\mathrm{O}_\mathrm{O}^\bullet}$	$E_{\mathrm{OH}_\mathrm{O}^\bullet}$	$E_{\mathrm{V}_\mathrm{O}^{\bullet\bullet}}$	$D^\circ_{\mathrm{O}_\mathrm{O}^\bullet}$	$D^\circ_{\mathrm{OH}_\mathrm{O}^\bullet}$	$D^\circ_{\mathrm{V}_\mathrm{O}^{\bullet\bullet}}$
	(kJ mol^{-1})			(m^2 s^{-1})	
65	35.09	67.00	1.62×10^{-04}	9.38×10^{-09}	1.30×10^{-08}
70	35.09	67.00	2.83×10^{-04}	9.38×10^{-09}	1.30×10^{-08}
75	35.09	67.00	4.96×10^{-04}	9.38×10^{-09}	1.30×10^{-08}
80	35.09	67.00	8.68×10^{-04}	9.38×10^{-09}	1.30×10^{-08}
85	35.09	67.00	1.52×10^{-03}	9.38×10^{-09}	1.30×10^{-08}
86	35.09	67.00	1.70×10^{-03}	9.38×10^{-09}	1.30×10^{-08}
90	35.09	67.00	2.66×10^{-03}	9.38×10^{-09}	1.30×10^{-08}

6 Recommended thermodynamic and transport parameters

Table 6 lists the recommended reaction enthalpies and entropies based on constrained fits the of the equilibrium conductivity measurements. Table 6 also lists the corresponding defect diffusion coefficients. These parameters respect all the constraints as discussed previously, including those suggested by the relaxation measurements. Note, for example, that the $\mathrm{O}_\mathrm{O}^\bullet$ diffusion coefficient at 800 °C is $D_{\mathrm{O}_\mathrm{O}^\bullet} = 1.11 \times 10^{-7}$ m^2 s^{-1}, which satisfies the constraint suggested from the ambipolar-diffusion analysis. As noted earlier, Fig. 4 compares the results of the constrained fits (solid lines) with the equilibrium conductivity measurements. Although the conductivity measurements are represented well over wide ranges of conditions and certain constraints are respected, the parameter set cannot be claimed to be unique. In fact, where possible, further experiments or theories are needed to unambiguously establish constraints.

6.1 Equilibrium defect concentrations

Using the recommended parameters, Fig. 7 shows equilibrium formula-unit concentrations of the three defects under dry and moist gas-phase environments. It is evident that $[\mathrm{V}_\mathrm{O}^{\bullet\bullet}]_\mathrm{L}$ and $[\mathrm{OH}_\mathrm{O}^\bullet]_\mathrm{L}$ depend only weakly on p_{O_2}, but depend strongly on temperature. By contrast, $[\mathrm{O}_\mathrm{O}^\bullet]_\mathrm{L}$ depends strongly on p_{O_2} in the oxidizing region, but nearly vanishes in the reducing environment.

Table 6 Recommended thermodynamic and transport parameters

Defect reaction thermodynamics

Reactions	ΔH° (kJ mol^{-1})	ΔS° (J mol^{-1} K^{-1})	K_p (750°C)
$\frac{1}{2}\mathrm{H}_2 + \mathrm{O}_\mathrm{O}^\bullet \rightleftharpoons \mathrm{OH}_\mathrm{O}^\bullet$	-146.01	-0.89	$2.56 \times 10^{+07}$
$\frac{1}{2}\mathrm{O}_2 + \mathrm{O}_\mathrm{O}^\times + \mathrm{V}_\mathrm{O}^{\bullet\bullet} \rightleftharpoons 2\mathrm{O}_\mathrm{O}^\bullet$	-36.08	-125.48	1.94×10^{-05}
$\mathrm{H}_2\mathrm{O} + \mathrm{V}_\mathrm{O}^{\bullet\bullet} + \mathrm{O}_\mathrm{O}^\times \rightleftharpoons 2\mathrm{OH}_\mathrm{O}^\bullet$	-80.00	-71.78	$2.16 \times 10^{+00}$
$\mathrm{H}_2 + \frac{1}{2}\mathrm{O}_2 \rightleftharpoons \mathrm{H}_2\mathrm{O}$	-248.11	-55.48	$5.87 \times 10^{+09}$

Charged-defect diffusion coefficients, $D_k = D_k^\circ \exp(-E_k/RT)$

	D_k° (m^2 s^{-1})	E_k (kJ mol^{-1})	D_k (600 °C) (m^2 s^{-1})	D_k (800 °C) (m^2 s^{-1})
$\mathrm{OH}_\mathrm{O}^\bullet$	9.39×10^{-9}	35.09	7.46×10^{-11}	1.84×10^{-10}
$\mathrm{V}_\mathrm{O}^{\bullet\bullet}$	1.30×10^{-8}	67.00	1.28×10^{-12}	7.12×10^{-12}
$\mathrm{O}_\mathrm{O}^\bullet$	1.70×10^{-3}	86.00	1.22×10^{-08}	1.11×10^{-07}

6.2 Dry oxygen conductivity

Although Fig. 4 reveals temperature dependencies over wide ranges of gas-phase environments, it can be difficult to read precise conditions from the typical log-log graphical representation. Figure 8 compares the measured and modeled conductivity as a function of reciprocal temperature in the dry O_2 environment (10 ppm of $\mathrm{H}_2\mathrm{O}$). The figure also shows model-predicted partial conductivities of the mobile-defect charge carriers. as well as the total conductivity as functions of temperature . In this highly oxidizing environment, the total conductivity is dominated by $\mathrm{O}_\mathrm{O}^\bullet$. However, even though the $\mathrm{H}_2\mathrm{O}$ concentration is very low, there is still some proton $\mathrm{OH}_\mathrm{O}^\bullet$ contribution at low temperature. The model-predicted $\mathrm{OH}_\mathrm{O}^\bullet$ partial conductivity is greater than the $\mathrm{V}_\mathrm{O}^{\bullet\bullet}$ partial conductivity at low temperature. However, above 600 °C, $\sigma_{\mathrm{V}_\mathrm{O}^{\bullet\bullet}}$ is larger than $\sigma_{\mathrm{OH}_\mathrm{O}^\bullet}$.

7 Surface kinetics and relaxation

As can be seen from Table 4, the predicted relaxation processes based on the equilibrium defect reactions at the rod surface are generally faster than the measured relaxation times. This strongly suggests that one or more surface reactions are kinetically rate-limiting. Using the thermodynamic and transport parameters shown in Table 6, the forward rate coefficients for the defect reactions ($k_{\mathrm{f,O_2}}$, $k_{\mathrm{f,H_2}}$, and $k_{\mathrm{f,H_2O}}$) are adjusted such that the model matches the measured relaxation histories. The three reverse rate expressions ($k_{\mathrm{b,O_2}}$, $k_{\mathrm{b,H_2}}$, and $k_{\mathrm{b,H_2O}}$) are evaluated based on Eqs. 20, 21, and 22 to maintain microscopic reversibility. Thus, the constrained-fit thermodynamic parameters are directly involved in the rate equations. Table 7 lists the reaction rate coefficients based on fitting the relaxation experiments.

Table 4 summarizes the measured and modeled characteristic relaxation times. Table 3 lists the relaxation end-point gas-phase mole-fraction compositions for the conductivity relaxations. Table 8 shows the corresponding three-pair ambipolar diffusivities, which assists in interpreting the relaxation behavior.

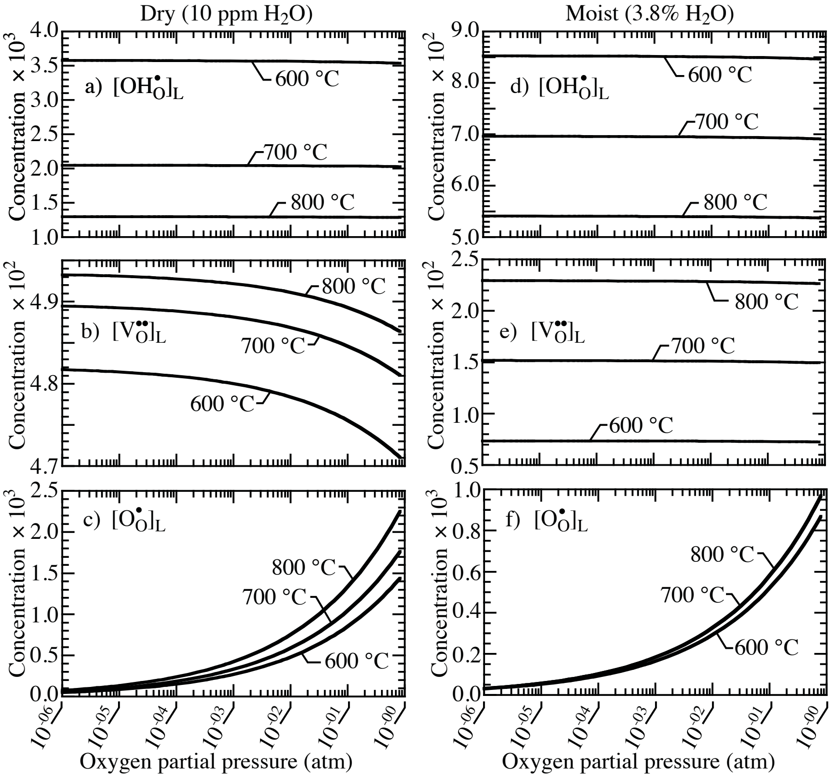

Fig. 7 Equilibrium defect concentrations (formula unit) as functions of oxygen partial pressure and temperature under dry and moist conditions.

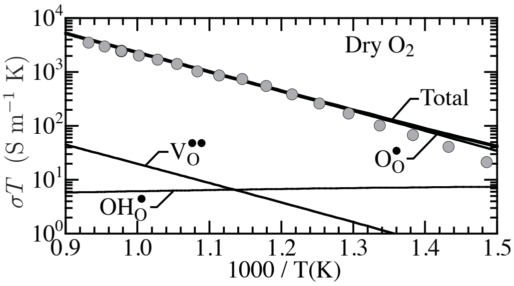

Fig. 8 Partial and total defect conductivities as functions of temperature in dry O_2 environment (10 ppm of H_2O). Filled circles are measurements and lines are model predictions.

The following sections include figures of the measured and modeled relaxation histories. Two factors are important in adjusting model parameters to achieve fits to the relaxation profiles. First is the characteristic relaxation time. Second is the qualitative functional form of the profiles. In some cases, although the characteristic time and shapes match well, it is evident from the plots that the end-

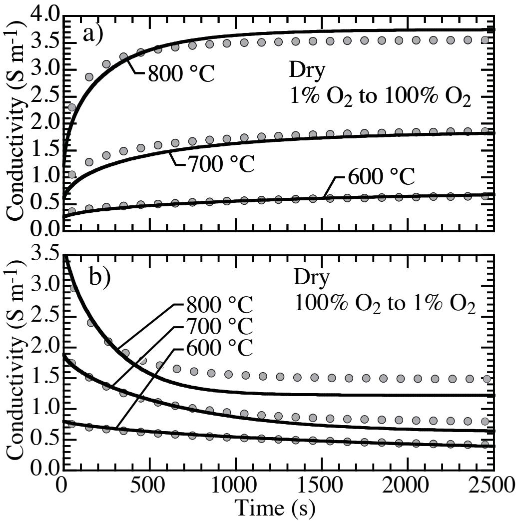

Fig. 9 Comparison of modeled (lines) and measured (points) conductivity relaxation histories under dry (10 ppm H_2O) conditions at three temperatures and $p = 0.829$ atm. a) Relaxation from 1% to 100% O_2. b) Relaxation from 100% to 1% O_2.

Table 7 Modified Arrhenius rate parameters for the defect-incorporation reactions, $k = AT^{\beta} \exp(-E_a/RT)$

	A (kmol, m, K)	β	E_a (kJ mol^{-1})
k_{f,O_2}	2.7087×10^{-05}	0.0	62.70
k_{f,H_2}	7.3995×10^{-02}	0.0	29.21
k_{f,H_2O}	1.8000×10^{-04}	0.0	0.00
k_{b,O_2}	$3.3922 \times 10^{+02}$	−0.5	98.77
k_{b,H_2}	2.8759×10^{-01}	−0.5	175.22
k_{b,H_2O}	$1.2327 \times 10^{+01}$	−1.0	80.00

point conductivities do not always fully align. Beginning with the equilibrium conductivity measurements, the full set of experiments took over two months to complete. During this time the sample rod was repeatedly oxidized and reduced, and heated and cooled. Inevitably, this repeated cycling caused some material degradation. Thus, there are small variations between the equilibrium end states for the relaxations and the initial equilibrium conductivity measurements for the same gas-phase environments (i.e., Fig. 4). Moreover, as is conventionally done, Fig. 4 shows conductivities on a logarithmic scale, which tends to diminish any scatter in the data.

7.1 Dry O_2

Figure 9a compares modeled and measured conductivity-relaxation histories from 1% O_2 to 100% O_2 under the dry environment at three temperatures and pressure of 0.829 atm (Table 3, DryOx). Figure 9b shows the corresponding reverse con-

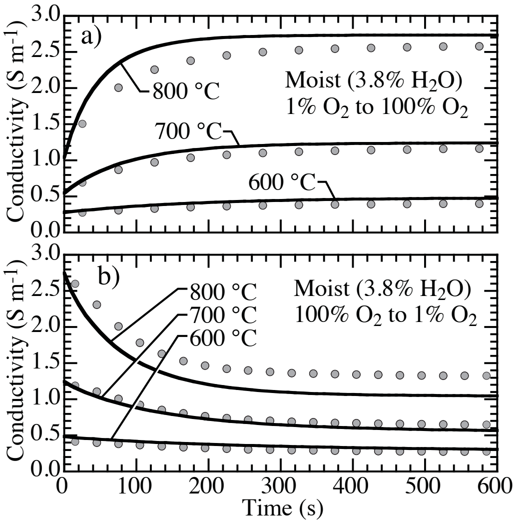

Fig. 10 Comparison of modeled (lines) and measured (points) conductivity relaxation histories under moist (3.8% H_2O) conditions at three temperatures and $p = 0.829$ atm. a) Relaxation from 1% to 100% O_2. b) Relaxation from 100% to 1% O_2.

Table 8 Comparison of ambipolar diffusion coefficients evaluated for different gas-phase environments

	T	**Reducing**			**Oxidizing**		
	(°C)	$\mathcal{D}_{\mathrm{O}_\mathrm{O}^\bullet-\mathrm{OH}_\mathrm{O}^\bullet}$	$\mathcal{D}_{\mathrm{O}_\mathrm{O}^\bullet-\mathrm{V}_\mathrm{O}^{\bullet\bullet}}$ (m^2 s^{-1})	$\mathcal{D}_{\mathrm{V}_\mathrm{O}^{\bullet\bullet}-\mathrm{OH}_\mathrm{O}^\bullet}$	$\mathcal{D}_{\mathrm{O}_\mathrm{O}^\bullet-\mathrm{OH}_\mathrm{O}^\bullet}$	$\mathcal{D}_{\mathrm{O}_\mathrm{O}^\bullet-\mathrm{V}_\mathrm{O}^{\bullet\bullet}}$ (m^2 s^{-1})	$\mathcal{D}_{\mathrm{V}_\mathrm{O}^{\bullet\bullet}-\mathrm{OH}_\mathrm{O}^\bullet}$
DryOx	600	4.32×10^{-10}	3.32×10^{-10}	3.64×10^{-11}	1.90×10^{-10}	1.07×10^{-10}	3.62×10^{-11}
	700	5.63×10^{-10}	1.11×10^{-09}	8.91×10^{-11}	2.63×10^{-10}	3.59×10^{-10}	8.90×10^{-11}
	800	6.99×10^{-10}	2.98×10^{-09}	1.58×10^{-10}	3.47×10^{-10}	9.60×10^{-10}	1.58×10^{-10}
MoistOx	600	7.99×10^{-09}	1.35×10^{-10}	1.70×10^{-12}	4.60×10^{-09}	4.37×10^{-11}	1.70×10^{-12}
	700	1.66×10^{-08}	6.40×10^{-10}	6.02×10^{-12}	7.32×10^{-09}	2.06×10^{-10}	6.00×10^{-12}
	800	2.51×10^{-08}	2.08×10^{-09}	1.80×10^{-11}	9.49×10^{-09}	6.69×10^{-10}	1.80×10^{-11}
MoistRedox	600	1.22×10^{-08}	1.22×10^{-08}	1.70×10^{-12}	4.60×10^{-09}	4.37×10^{-11}	1.70×10^{-12}
	700	4.12×10^{-08}	4.11×10^{-08}	6.02×10^{-12}	7.32×10^{-09}	2.06×10^{-10}	6.00×10^{-12}
	800	1.11×10^{-07}	1.10×10^{-07}	1.80×10^{-11}	9.49×10^{-09}	6.69×10^{-10}	1.80×10^{-11}

ductivity relaxation histories. It is apparent that the measured relaxation histories can be reasonably well predicted with the kinetic-limited relaxation model. The magnitudes of the effective ambipolar diffusion coefficients can add additional insight.

The ambipolar diffusion coefficient $\mathcal{D}_{\mathrm{O}_\mathrm{O}^\bullet-\mathrm{V}_\mathrm{O}^{\bullet\bullet}}$ is larger than $\mathcal{D}_{\mathrm{O}_\mathrm{O}^\bullet-\mathrm{OH}_\mathrm{O}^\bullet}$ at the 700 and 800 °C, but $\mathcal{D}_{\mathrm{O}_\mathrm{O}^\bullet-\mathrm{V}_\mathrm{O}^{\bullet\bullet}}$ becomes smaller than $\mathcal{D}_{\mathrm{O}_\mathrm{O}^\bullet-\mathrm{OH}_\mathrm{O}^\bullet}$ at 600 °C, even though there is only about 10 ppm of H_2O (cf., Table 8). Therefore, the relaxation time under the equilibrated-surface assumption is determined by $\mathcal{D}_{\mathrm{O}_\mathrm{O}^\bullet-\mathrm{V}_\mathrm{O}^{\bullet\bullet}}$ at 700 and 800 °C, but by $\mathcal{D}_{\mathrm{O}_\mathrm{O}^\bullet-\mathrm{OH}_\mathrm{O}^\bullet}$ at 600 °C. Because $\mathcal{D}_{\mathrm{O}_\mathrm{O}^\bullet-\mathrm{V}_\mathrm{O}^{\bullet\bullet}}$ and $\mathcal{D}_{\mathrm{O}_\mathrm{O}^\bullet-\mathrm{OH}_\mathrm{O}^\bullet}$ at 1% O_2 are larger than they are at 100% O_2, it is reasonable that the relaxation time with equilibrium surface reactions from 100% O_2 to 1% O_2 is shorter than it is at 1% O_2 to 100% O_2 (cf., Table 4).

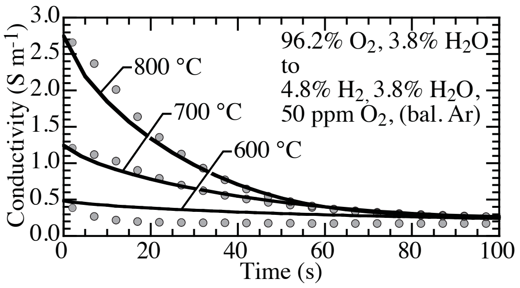

Fig. 11 Comparison of model-predicted conductivity relaxation histories (lines) and the experimental measurements (filled circles) from 100% O_2 to 5% H_2 under moist conditions at three temperatures and pressure of 0.829 atm.

Table 4 and also Fig. 9 show that the relaxation times from 1% O_2 to 100% O_2 are significantly shorter than they are from 100% O_2 to 1% O_2 at the same temperatures. The relatively fast relaxation is the result of relatively faster defect transport. However, the actual relaxation time is limited by the kinetics associated with rate-limiting surface kinetics. In the dry O_2 environment, the dominant rate-limiting step is the O_2 incorporation. The relaxation time predicted by the kinetic model is consistent with the experimental observations.

7.2 Moist O_2

Figure 10a shows that the measured conductivity-relaxation histories between 1% O_2 and 100% O_2 under a saturated moist environment (Table 3, MoistOx) can also be predicted reasonably well by the kinetic model. In the moist environment, Table 8 shows that the ambipolar diffusion coefficient $\mathcal{D}_{\mathrm{O}_\mathrm{O}^\bullet-\mathrm{OH}_\mathrm{O}^\bullet}$ is much larger than $\mathcal{D}_{\mathrm{O}_\mathrm{O}^\bullet-\mathrm{V}_\mathrm{O}^{\bullet\bullet}}$ at all the three temperatures. Therefore, the defect transport is associated primarily with $\mathrm{O}_\mathrm{O}^\bullet$ and $\mathrm{OH}_\mathrm{O}^\bullet$. Compared with the dry O_2 case, $\mathcal{D}_{\mathrm{O}_\mathrm{O}^\bullet-\mathrm{OH}_\mathrm{O}^\bullet}$ is also much larger in the moist environment. Thus, the relaxation time for the moist O_2 is much shorter than it is under dry conditions. However, the dominant rate-limiting step remains the O_2 incorporation.

7.3 Moist H_2-O_2

Figure 11 illustrates that the measured conductivity relaxation from 100% O_2 to 5% H_2 in a moist environment (Table 3, MoistRedox) can be represented well by the NPP model considering the surface kinetics. In the highly reduced environment, the ambipolar diffusivity $\mathcal{D}_{\mathrm{O}_\mathrm{O}^\bullet-\mathrm{OH}_\mathrm{O}^\bullet}$ is almost equal to $\mathcal{D}_{\mathrm{O}_\mathrm{O}^\bullet-\mathrm{V}_\mathrm{O}^{\bullet\bullet}}$, but much larger than it is under the dry and moist oxidizing environment shown in Table 8. Therefore, the relaxation time from the oxidizing to reducing environment is very short (cf., Table 4). In the reducing environment, the surface kinetics is dominated by the H_2 incorporation rate.

8 Summary and conclusions

A combination of equilibrium-conductivity and conductivity-relaxation measurements, together with model-based interpretation, is used to establish thermodynamic and transport properties for 10% yttrium-doped barium zirconate (BZY10). Specifically, enthalpy and entropy changes (ΔH° and ΔS°) are reported for reactions representing the incorporation of H_2, O_2, and H_2O. The transport properties are reported in terms of pre-exponential factors and activation energies for the diffusion coefficients of three mobile defects (oxygen vacancies $V_O^{\bullet\bullet}$, protons $OH_O^{\bullet}$, and O-site polarons $O_O^{\bullet}$). The equilibrium conductivities are measured using alternating-current impedance spectroscopy. The relaxation measurements consider switching the gas-phase environments rapidly from high to low oxygen partial pressures, and vice versa. The conductivity during relaxation is measured using impedance at a single frequency, which was selected based on measuring the same resistance as the full EIS sweeps at the asymptotic equilibrium end states. To model the relaxation experiments and considering three mobile charge carriers, the relaxation problem is solved computationally using a Nernst–Planck–Poisson formulation. The relaxation modeling incorporates the possibility of kinetic rate limitations of the surface reactions, but requires microscopic reversibility that is consistent with the equilibrium thermodynamics. Although not claimed to be entirely unique, the properties reported here are consistent with prior literature, the equilibrium and relaxation experiments, and physical constraints. Thus, complete and self-consistent set of properties is probably the best that is currently available for BZY10.

9 Acknowledgements

This research was supported by the Office of Naval Research via grant N00014-08-1-0539 and the Colorado School of Mines Foundation, Protonic Capital Funds. We gratefully acknowledge insightful and helpful discussions with Profs. Ryan O'Hayre, Greg Jackson, and Neal Sullivan (CSM). We are also grateful for the efforts of Dr. Anthony Manerbino (CoorsTek), who prepared the BZY10 rods used in the experiments.

References

1 W. Coors, *J. Power Sources*, 2003, **118**, 150–156.

2 M. Ni, D. Leung and M. Leung, *J. Power Sources*, 2008, **183**, 133–142.

3 C. Zamfirescu and I. Dincer, *Thermochimica Acta*, 2009, **486**, 32–40.

4 A. Arpornwichanop and Y. Patcharavorachot, *Chem. Engr. Res. and Design*, 2013, **91**, 1508–1516.

5 W. Li, R. Borry and E. Iglesia, *Chem. Eng. Sci.*, 2002, **57**, 4595–4604.

6 W. Coors, *J. Electrochem. Soc.*, 2004, **151**, A994–A997.

7 W. Coors, *Solid State Ionics*, 2007, **178**, 481–485.

8 I. Riess, *Solid State Ionics*, 2003, **157**, 1–17.

9 W. Lai and S. Haile, *Phys. Chem. Chem. Phys.*, 2008, **10**, 865–883.

10 R. Kee, H. Zhu, B. Hildenbrand, E. Vøllestad, M. Sanders and R. O'Hayre, *J. Electrochem. Soc.*, 2013, **160**, F290–F300.

11 M. Sanders, H. Zhu, R. Kee and R. O'Hayre, *Solid State Ionics*, 2013, **249250**, 6–16.

12 E. Vøllestad, H. Zhu and R. Kee, *J. Electrochem. Soc.*, 2014, **161**, F114–F124.

13 S. Ricote, H. Zhu, W. Coors, C. Chatzichristodoulou and R. Kee, *Solid State Ionics*, 2014, **265**, 22–28.

14 H. Zhu, S. Ricote, W. Coors, C. Chatzichristodoulou and R. Kee, *Solid State Ionics*, 2014, **268**, 198–207.

15 S. Stokes and M. Islam, *J. Mater. Chem.*, 2010, **20**, 6258–6264.

16 K. Kreuer, S. Adams, W. Munch, A. Fuchs, U. Klock and J. Maier, *Solid State Ionics*, 2001, **145**, 295–306.

17 K. Kreuer, *Annu. Rev. Mater. Res.*, 2003, **33**, 333–359.

18 C. Kjolseth, L. Wang, R. Haugsrud and T. Norby, *Solid State Ionics*, 2010, **181**, 1740–1745.

19 E. Bévillon, G. Dezanneau and G. Geneste, *Phys. Rev. B*, 2011, **83**, 174101.

20 J. Hermet, F. Bottin, G. Dezanneau and G. Geneste, *Phys. Rev. B*, 2012, **85**, 205137.